Sea Level Expression of Intrinsic and Forced Ocean Variabilities at Interannual Time Scales

Thierry Penduff, Mélanie Juza, Bernard Barnier, Jan D. Zika, William K. Dewar, Anne-Marie Tréguier, Jean-Marc Molines, Nicole Audiffren

Sea Level Expression of Intrinsic and Forced Ocean Variabilities at Interannual Time Scales

THIERRY PENDUFF,*,+ MÉLANIE JUZA,* BERNARD BARNIER,* JAN ZIKA,* WILLIAM K. DEWAR,+ ANNE-MARIE TREGUIER,# JEAN-MARC MOLINES,* AND NICOLE AUDIFFREN@

* *Laboratoire des Ecoulements Géophysiques et Industriels, UMR CNRS 5519, Université de Grenoble, Grenoble, France*
+ *Earth, Ocean and Atmospheric Science Department, The Florida State University, Tallahassee, Florida*
# *Laboratoire de Physique des Océans, UMR CNRS 6523, IFREMER, UBO, Plouzané, France*
@ *Centre Informatique National de l'Enseignement Supérieur, Montpellier, France*

This paper evaluates in a realistic context the local contributions of direct atmospheric forcing and intrinsic oceanic processes on interannual sea level anomalies (SLAs). A 1/4° global ocean–sea ice general circulation model, driven over 47 yr by the full range of atmospheric time scales, is quantitatively assessed against altimetry and shown to reproduce most observed features of the interannual SLA variability from 1993 to 2004. Comparing this simulation with a second driven only by the climatological annual cycle reveals that the intrinsic part of the total interannual SLA variance exceeds 40% over half of the open-ocean area and exceeds 80% over one-fifth of it. This intrinsic contribution is particularly strong in eddy-active regions (more than 70%–80% in the Southern Ocean and western boundary current extensions) as predicted by idealized studies, as well as within the 20°–35° latitude bands. The atmosphere directly forces most of the interannual SLA variance at low latitudes and in most midlatitude eastern basins, in particular north of about 40°N in the Pacific. The interannual SLA variance is almost entirely due to intrinsic processes south of the Antarctic Circumpolar Current in the Indian Ocean sector, while half of this variance is forced by the atmosphere north of it. The same simulations were performed and analyzed at 2° resolution as well: switching to this laminar regime yields a comparable forced variability (large-scale distribution and magnitude) but almost suppresses the intrinsic variability. This likely explains why laminar ocean models largely underestimate the interannual SLA variance.

1. Introduction

a. Context

The dynamical response of the nonlinear ocean to the atmospheric variability is complex: dynamical system approaches and diagnostics of potential vorticity balances have demonstrated that in presence of stochastic, seasonal, or constant atmospheric forcing, oceanic nonlinearity can intrinsically generate and sustain variability of the horizontal circulation at interannual time scales (e.g., Jiang et al. 1995; Spall 1996; Berloff and McWilliams 1999; Hazeleger and Drijfhout 2000; Dewar 2001; Cessi and Louazel 2001; Wirth et al. 2002; Dewar 2003; Simonnet et al. 2003, 2005; Hogg and Blundell 2006; Berloff et al. 2007). There are various manifestations of this variability, including, for example, fluctuations of inertial gyres and associated mode water pools, western boundary current transitions between high- and low-energy states (studied in closed basins), slow vacillations of turbulent jets, and eddy-induced modulations of topographic steering (studied in periodic channels). In this study we focus on the interannual variability of the near-surface horizontal circulation [see section 2 in Dijkstra and Ghil (2005) for a review of idealized results], which differs from the (slower) variability of the thermohaline circulation (their section 3).

The studies mentioned above made use of numerical models with simplified dynamics (e.g., quasigeostrophic or shallow water, often flat bottomed and/or barotropic) and geometries, resolving a limited range of processes. Such idealized approaches are necessary to perform detailed analyses of key interactions and to demonstrate their possible existence in the real ocean. These results provide important dynamical insights, but they cannot

Corresponding author address: Thierry Penduff, LEGI-MEOM, BP53, 38041 Grenoble CEDEX 9, France.
E-mail: thierry.penduff@legi.grenoble-inp.fr

be directly compared with actual observations regarding the distribution and magnitude of the intrinsic variability in the real ocean.

Regional and basin-scale manifestations of intrinsic low-frequency (LF) variability have also been reported in seasonally forced eddying simulations based on ocean general circulation models (OGCMs) that solve the primitive equations within realistic geometries with realistic initial states. These studies have revealed significant interannual-to-decadal modulations of, for example, basin-averaged mesoscale activity (Penduff et al. 2004), intergyre heat transport (Hall et al. 2004), sea level variability (Cabanes et al. 2006), expansion–contraction of western boundary current systems (Taguchi et al. 2007), and meridional overturning circulation (Biastoch et al. 2008).

Both idealized and more ''realistic'' model studies suggest that at high Reynolds number and with a sufficiently strong atmospheric forcing, the oceanic variability is likely a complex combination of direct responses to the atmosphere, and of intrinsic fluctuations (Dijkstra and Ghil 2005). However, the interplay between forced and intrinsic variabilities and their relative contributions to the observed interannual variability remain unclear. For instance, the Kuroshio undergoes realistic interannual variability patterns both in wind-driven laminar models (Qiu 2003) and in constantly forced eddying models (Pierini 2006); Taguchi et al. (2007) suggests from more realistic simulations that the observed variability arises from the atmospheric forcing of intrinsic variability modes. In other words, the contributions of forced and intrinsic interannual variabilities to the observed signals and their possible interactions may largely depend on location, but they have been mostly investigated regionally and in idealized frameworks so far.

b. This study

To our knowledge, no dedicated mapping and description of intrinsic and forced variabilities have been yet attempted at global scale with comparisons to observations. This paper addresses three main issues in the (still simplified) context of global ocean–sea ice primitive equation dynamics with realistic geometry, and from the perspective of the (well observed) sea level variability:

- What are the contributions of the forced and intrinsic components in the interannual sea level anomaly (SLA) variability?
- How are these contributions distributed spatially at global scale?
- What is the sensitivity of intrinsic interannual variability to mesoscale activity?

Our aim is to qualitatively (and perhaps quantitatively) evaluate the relative contributions of forced and intrinsic interannual variabilities in the global ocean as measured by altimeters (at the expense of detailed process analyses). This complements process-oriented studies where individual dynamical processes are studied in detail in highly idealized contexts (at the expense of direct comparisons with actual observations). We first evaluate against altimeter observations a ''pivot'' experiment, that is, a state-of-the-art, 47-yr eddy-admitting (1/4°) ocean–sea ice global simulation forced by a realistic interannual forcing. This evaluation follows the approach proposed by Penduff et al. (2010, hereafter P10). The same model is then driven by the mean annual cycle only to isolate the intrinsic interannual component; the variance of the forced component is then estimated from the latter two simulations. To illustrate the possible contribution of nonlinearities on these components, the latter comparison is also made between coarse-resolution (2°), laminar versions of the interannually and seasonally forced experiments.

Archiving, Validation, and Interpretation of Satellite Oceanographic data (AVISO) is the only existing dataset that allows a relatively long-term, global, and local description of the range of scales we are focused on. We shall therefore focus our analyses on SLAs. The detailed investigation of unobserved variables and underlying processes in individual regions and simulations would require, in turn, a number of idealized studies, which are left for the future.

Section 2 presents the 2° and 1/4° model configurations, the interannual and seasonal forcing functions, the construction of our collocated multimodel and observed SLA dataset, and comparison procedures. Our pivot experiment (1/4°, interannual forcing) is assessed against SLA observations in section 3. In section 4, we compare this simulation with its seasonally forced counterpart to describe the features of intrinsic and forced interannual SLA variabilities at global scale. Both 2° simulations are compared in section 5 to estimate the possible contribution of nonlinearities at finer resolution. Conclusions are given and discussed in section 6.

2. Models, datasets, and comparison procedures

a. Model simulations

The six global ocean–sea ice model simulations mentioned in this paper were performed in the framework of the Drakkar project (http://www.ifremer.fr/lpo/drakkar/), using the Nucleus for European Modelling of the Ocean (NEMO) code (Madec et al. 2008). Figure 1 summarizes the relationships between these simulations. Our sensitivity studies to the forcing were performed using

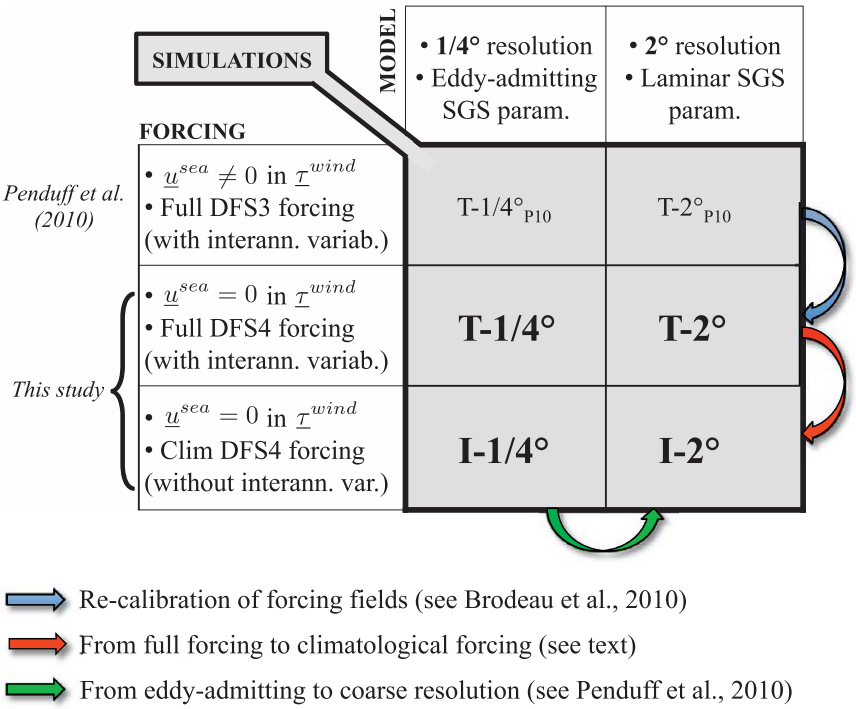

FIG. 1. Summary of the model simulations mentioned in this study, including P10 simulations and those in bold form the core of the present paper. Note that all model parameters except atmospheric fields and bulk formulas remain unchanged within each column and everything except resolution and subgrid-scale parameterizations remain unchanged within each row. The three curved arrows, and associated descriptions below the matrix, summarize configurations changes between successive lines or columns.

eddy-admitting (¼°) and laminar (2°) configurations. Their forcings aside, these configurations are exactly the same as those described in P10; they differ from each other in terms of horizontal resolution (2° and ¼°) and subgrid-scale parameterizations. Note that the meridional resolution of the 2° grid gets finer toward the equator, where it reaches ⅓°; this explains why the ¼° and 2° simulations do not differ much in this region. The ¼° and 2° configurations are driven by two forcing functions, yielding a total of four simulations.

1) *T* FORCING

The first forcing function, labeled *T* since it drives the *total* low-frequency variability (forced plus intrinsic), is based on reanalyzed atmospheric fields and satellite data, and covers the period 1958–2004. It is described in detail [and referred to as Drakkar forcing set 4.1 (DFS4.1)] in Brodeau et al. (2010). In short, DFS4 is based on satellite-derived monthly precipitations, daily radiative heat fluxes, and 6-hourly 10-m atmospheric state variables from European Centre for Medium-Range Weather Forecasts (ECMWF) fields [40-yr ECMWF Re-Analysis (ERA-40) before 2002, ECMWF analysis afterward]. Turbulent air–sea and air–ice fluxes are computed from ECMWF variables and surface model variables through bulk formulas. This forcing function is used to drive the $T-2°$ and $T-¼°$ simulations.

To keep the paper concise, the assessment of $T-2°$ and $T-¼°$ against altimetry will involve comparisons with two earlier simulations, labeled $T-2°_{P10}$ and $T-¼°_{P10}$, respectively, in the following. These were extensively described and evaluated in P10. Simulations $T-2°$ and $T-¼°$ only differ from these earlier simulations by two features of their forcing function. First, the atmospheric fields (DFS3) used to drive the P10 runs have been updated in $T-2°$ and $T-¼°$.[1] Second, the bulk formulas in $T-2°$ and $T-¼°$ (as well as in $I-2°$ and $I-¼°$, described below) do not take into account surface currents in the computation of wind stress,

[1] The calibration of atmospheric variables has been improved from DFS3 to DFS4, and some spurious discontinuities have been removed. The rationale, description, and oceanic impact of individual changes made from DFS3 to DFS4 are discussed in detail in Brodeau et al. (2010).

unlike in P10 simulations. This current–stress feedback has been discussed since Pacanowski (1987), but there is still no clear consensus yet on whether and how it should be parameterized in numerical models [see in particular Eden and Dietze (2009), and references therein]. To maximize the consistency between this *T* forcing and the seasonal *I* forcing needed for this study, we chose to ignore this latter feedback in the computation of wind stresses (see the section below).

2) I FORCING

The second forcing function was built to preserve the daily mean annual cycle and long-term average of the *T* forcing, but it is devoid of interannual variability; it is labeled *I* since only *intrinsic* low-frequency variability may be excited. This forcing was built by computing 365 daily averages (i.e., a daily mean annual climatology) of 6-hourly DFS4 variables during 50 yr. This daily annual climatology includes precipitations, runoff, radiative fluxes, atmospheric state variables (air temperature, air humidity, wind speed vector $\mathbf{u}_{\text{air}}$), and the main quadratic contributions to air–sea fluxes: bulk exchange coefficients (C_d for momentum, C_e for latent fluxes, and C_h for sensible heat fluxes) and pseudowind stresses $C_d|\mathbf{u}_{\text{air}}|u_{\text{air}}$. As mentioned above, ocean currents are not used to calculate wind stresses. The resulting *I* forcing fields were then low-pass filtered in time (three-point Hanning filter) to remove the remaining, although small, high-frequency (HF) noise. This *I* forcing function is applied for 314 yr on the 2° and ¼° configurations. It is devoid of any interannual atmospheric variability and of intraseasonal synoptic transients. The corresponding simulations will be referred to as $I - 2°$ and $I - ¼°$, respectively.

This method ensures that the linear and the main quadratic air–sea flux terms (stability of the atmospheric boundary layer, exchange coefficients, wind stresses, turbulent heat and freshwater fluxes, etc.) have the same seasonal cycles and long-term means in the *T* and *I* forcing functions. In other words, this method maximizes the consistency between the interannual and seasonal forcing functions, and between our simulations.

To summarize, the four new simulations investigated in this paper[2] are $T - 2°$, $T - ¼°$, $I - 2°$, and $I - ¼°$. When joined with the two P10 simulations, we have a total of six global runs. Model fields, including sea surface height (SSH), were saved as successive 5-day averages throughout both interannually forced 47-yr simulations. Model fields were saved at the same 5-day rate after year 300 in both 314-yr seasonally forced simulations but as monthly averages before this. Our choice of outputs and associated constraints are described in appendix A.

b. Sea level datasets

The collocation and filtering process of simulated and observed SLAs is presented in detail in P10 (their section 2.2.1); only a short summary is given here. Our observational reference is the 1993–2004 series of altimeter sea level anomalies, provided by AVISO as a series of global weekly maps on a ⅓° × ⅓° Mercator grid. Simulated SSHs are converted into SLA maps after a time–space collocation onto this AVISO dataset. The resulting dataset consists of weekly maps of observed (AVISO) and simulated SLAs available on the same ⅓° Mercator grid, on the same dates (the case of seasonally forced simulations is presented in appendix A). This seven-member (AVISO + six simulations) ''raw'' SLA dataset is then filtered in time using a Lanczos filter. As done and described in P10, each member of this raw dataset is split into its ''low frequency'' (time scales longer than 18 months) and ''high frequency'' (time scales shorter than 5 months) parts.[3] In the present study, linear trends are removed at each grid point from each LF dataset (see appendix B).

c. Comparison statistics

Our purpose is to characterize at high and low frequency (the main focus being on the latter) the distribution and magnitude of SLA variability in our seven collocated sources, that is, AVISO, the four new simulations, and the two P10 simulations. The processing summarized below is described in detail in P10 (their section 2.2.2).

1) σ, CT, AND CS

For each of these 14 cases (7 datasets × 2 frequency bands), we compute 2D fields of SLA temporal standard deviations [$\sigma(i, j)$]. The σ maps are shown in log scale as gray shadings (low frequency) and contours (high frequency) for AVISO and the four recent runs in Figs. 2 and 3 after spatial smoothing for clarity. The reader is referred to P10's Fig. 4 for σ maps in the $T - 2°_{\text{P10}}$ and $T - ¼°_{\text{P10}}$ simulations.

For both frequency bands and each simulation (12 cases), we compute maps of correlation coefficients Ct(i, j)

[2] For clear reference, these four simulations are referred to as ORCA246-G83b, ORCA025-B83, ORCA246-MJM01, and ORCA025-MJM01 in the Drakkar database.

[3] LF and HF frequency bands will also be referred to as ''interannual'' and ''mesoscale,'' respectively, as in P10. Time scales between 5 and 18 months (referred to as *quasi annual* in P10) are barely sensitive to the shutoff of interannual forcing and are not investigated in the present study.

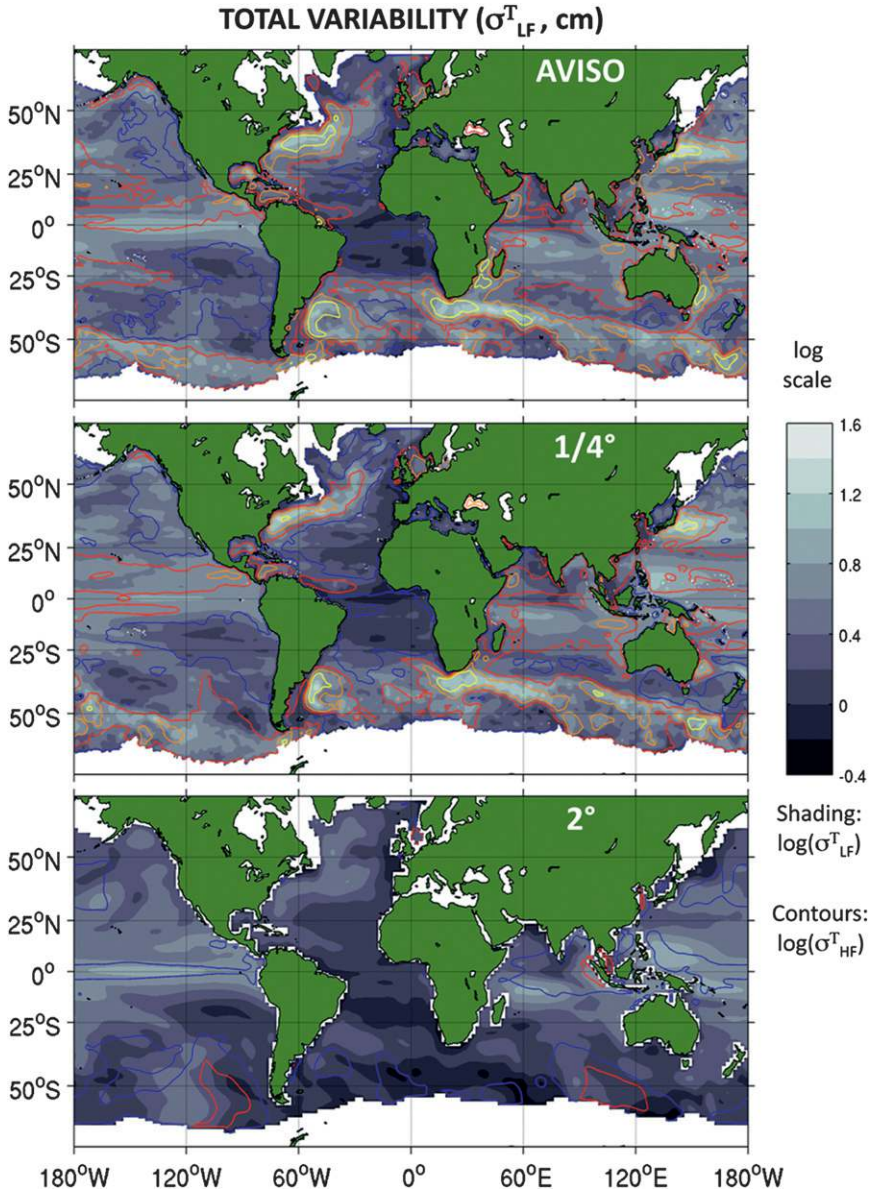

FIG. 2. Total variability (log scale, cm) at LF (gray shading) and HF (selected contours: 0.2 in blue, 0.5 in red, 0.8 in orange, 1.1 in yellow): (top) AVISO, and fully forced model simulations at (middle) 1/4° and (bottom) 2°. For clarity, maps have been smoothed.

between (observed and simulated) collocated local SLA time series. Local significance levels at 95% are estimated at each grid point for each Ct(i, j) map from lagged autocorrelations functions of observed and simulated SLA time series, as proposed by von Storch and Zwiers (1999). As noted by P10, these significance level estimates are relevant for our time series, which have different (and arbitrary) spectra and autocorrelations. Insignificant Ct(i, j) values are masked in the following: only significant Ct(i, j) values are considered in further computations and discussed below.

Statistics will also be presented within 14 latitude bands labeled $\lambda \in (1; 14)$, spanning the 70°S–70°N latitude range by 10° intervals (this interval was 5° in P10). To this aim, the 14 $\sigma(i, j)$ and 12 Ct(i, j) maps are simply area weighted and averaged over each band to yield $\sigma(\lambda)$ and Ct(λ) in each frequency band. The spatial correlation Cs(λ) between simulated $\sigma(i, j)$ maps and their AVISO counterpart is computed within each latitude band for all 12 cases to evaluate the agreement between both variability maps as a function of latitude. These latitude-dependent skill estimates are presented for the earlier

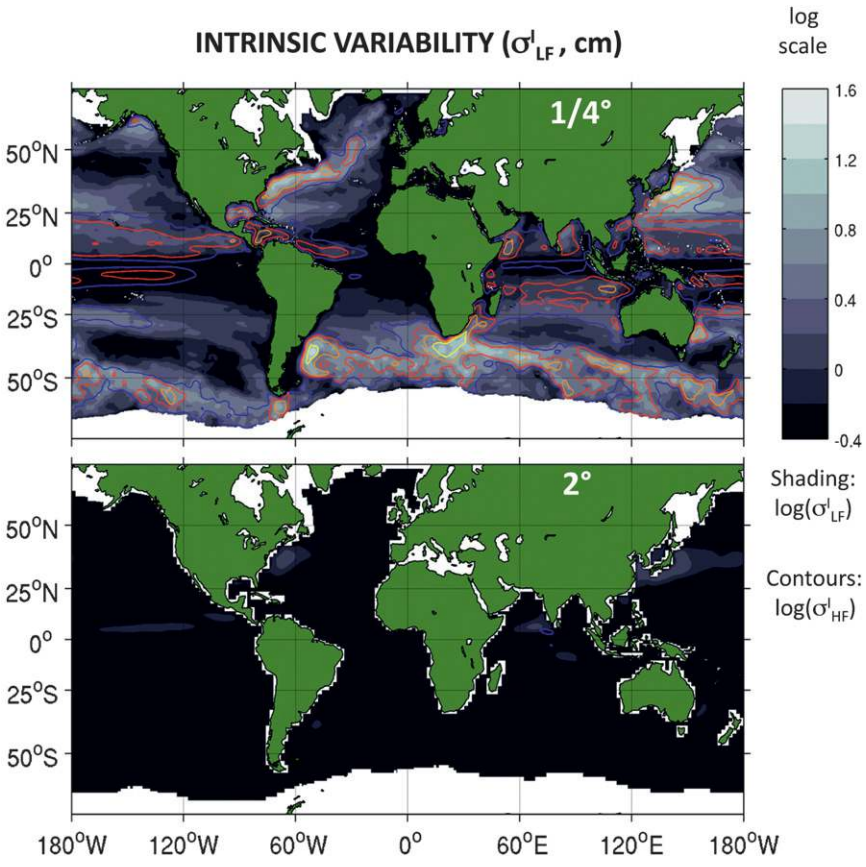

FIG. 3. As in Fig. 2, but for intrinsic variability obtained from seasonally forced simulations (top) $I - 1/4°$ and (bottom) $I - 2°$.

($T - 1/4°_{P10}$, $T - 2°_{P10}$) and new ($T - 1/4°$, $T - 2°$) interannually forced simulations in Fig. 5, and for the interannually forced ($T - 1/4°$ and $T - 2°$) and seasonally forced ($I - 1/4°$ and $I - 2°$) new simulations in Fig. 6.

The agreement between (unsmoothed) LF and HF variability maps within each individual dataset is evaluated from spatial correlations in successive latitude bands, and shown in Fig. 4 for AVISO and for the four new simulations.

2) Intrinsic and forced LF variability

We shall consider in this study that at low frequency, the total SLA variability $T(t)$ locally found in interannually forced simulations T is the sum of the intrinsic component $I(t)$ (diagnosed from I simulations) and of a forced variability component $F(t)$. This simple assumption is tacitly made in idealized studies, where the low-frequency variability simulated under steady or seasonal forcing is considered representative of the intrinsic component of the oceanic variability. This yields the following relationship between the total, intrinsic, and forced local LF variances:

$$(\sigma^T)^2 = (\sigma^I)^2 + (\sigma^F)^2 + 2\sigma^I\sigma^F C_{I,F}, \qquad (1)$$

where $C_{I,F}$ denotes the local temporal correlation between intrinsic and forced SLA fluctuations. As mentioned in the introduction, idealized studies have shown that $I(t)$ has a strong random character; in other words, we also assume at this point that the local time series of $I(t)$ and $F(t)$ at low frequency are not significantly correlated in time (i.e., $C_{I,F} \sim 0$; the validity of this convenient, initial assumption[4] is assessed and discussed in section 4c(1)]. This second assumption allows us to estimate the local variance of *forced* low-frequency SLA variabilities as the difference between total and intrinsic LF variances. The forced LF standard deviation of SLA

[4] This assumption was explicitly made by Hazeleger and Drijfhout (2000, p. 13 966), who wrote, "By definition, externally generated oceanic variability is generated independently of oceanic processes, for instance, the passive response of the ocean to variability in the atmospheric forcing."

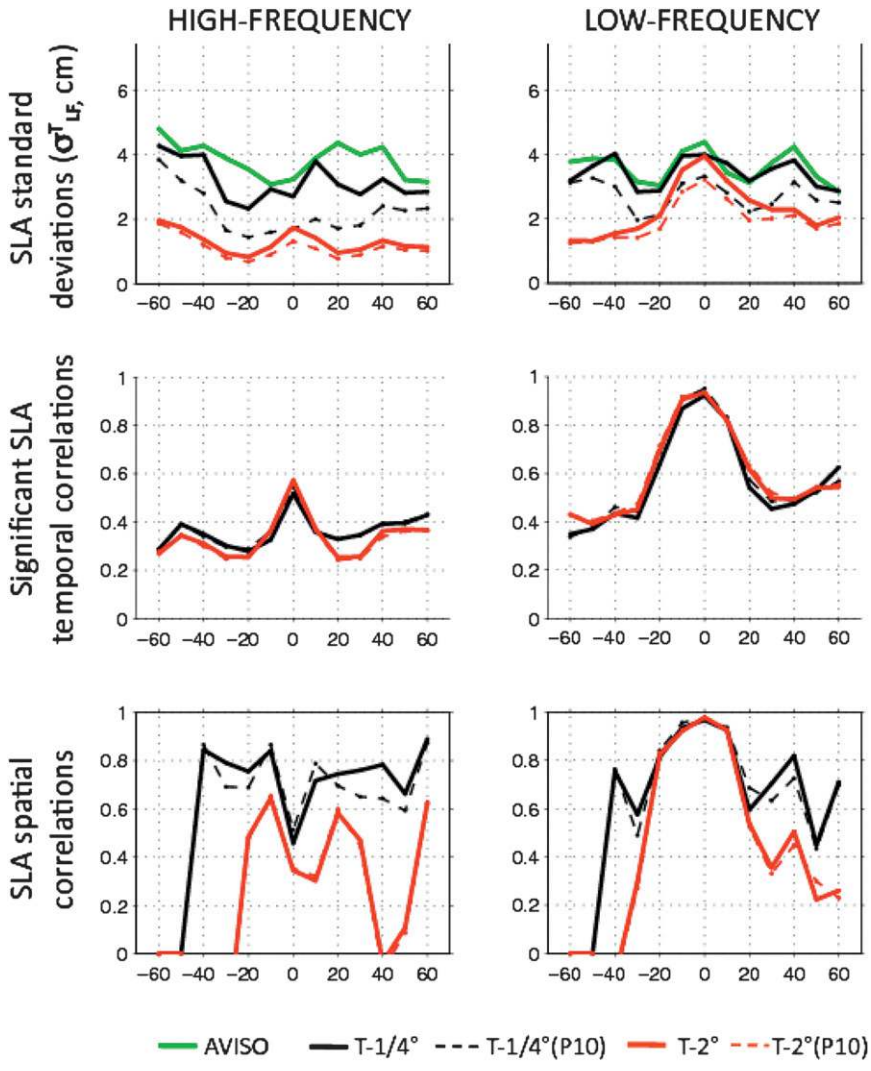

FIG. 4. Skills of earlier ($T - 1/4°_{P10}$ and $T - 2°_{P10}$, dashed lines) and new ($T - 1/4°$ and $T - 2°$, solid lines) fully forced simulations as a function of latitude (abscissas) in the (left) HF and (right) LF frequency bands. (top row) Total SLA standard deviation [$\sigma^T(\lambda)$, cm]; AVISO reference is shown in green. (middle row) Significant temporal correlations with local AVISO time series [Ct(λ)]. (bottom row) Spatial correlations [Cs(λ)] between simulated and observed $\sigma^T(i, j)$ maps.

in the eddying regime may thus be estimated at every grid point by

$$\sigma^{F-1/4°}_{LF} = \sqrt{(\sigma^{T-1/4°}_{LF})^2 - (\sigma^{I-1/4°}_{LF})^2}.$$

This latter quantity, and its laminar counterpart $\sigma^{F-2°}_{LF}$ (derived from $\sigma^{T-2°}_{LF}$ and $\sigma^{I-2°}_{LF}$), are shown as maps and in zonal average in Fig. 7. Finally, the percentage of the total LF variance that is generated intrinsically is estimated as

$$R^I_{LF} = 100\% \times (\sigma^I_{LF}/\sigma^T_{LF})^2.$$

These ratios are shown as maps and zonal averages in Fig. 8 for the 1/4° and 2° resolutions.

3. Assessment of SLA variability in the pivot experiment $T - 1/4°$

We first assess with respect to AVISO the geographical distribution, magnitude, and phase of the SLA variability in the 1/4° interannually forced simulation ($T - 1/4°$) between 1993 and 2004. The (smoothed) spatial distributions of high- and low-frequency variability in both datasets are shown in the top and middle panels of Fig. 2. Besides the recalibration of its forcing (see Fig. 1), the

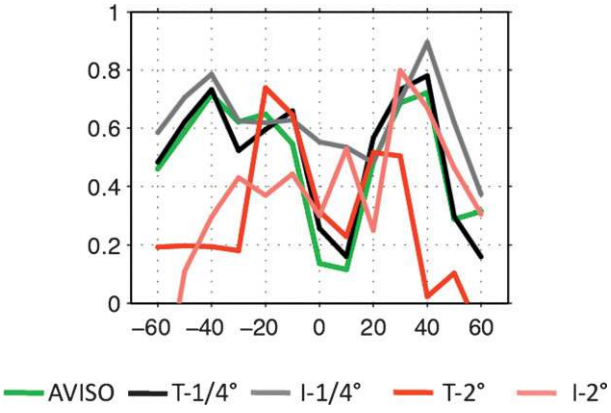

FIG. 5. Spatial correlations by latitude band (abscissas) between unsmoothed HF and LF $\sigma(i, j)$ maps for each dataset (colors); large values mean large correspondence between spatial structures of σ in both frequency bands.

$T - 1/4°$ simulation is the same as $T - 1/4°_{P10}$ which was extensively compared to the same AVISO referenced by P10. For conciseness, the fidelity of $T - 1/4°$ with respect to AVISO is not discussed as extensively here but is compared to $T - 1/4°_{P10}$ in zonal average (plain and dashed black lines in Fig. 5); in addition to this figure, the interested reader is referred to P10 for an in-depth description of the strengths and weaknesses of $T - 1/4°_{P10}$.

a. HF variability at ¼°

The middle left panel in Fig. 5 shows in zonal average that the temporal correlations between observed and local HF time series are almost identical in $T - 1/4°$ and $T - 1/4°_{P10}$. However, the transition from $T - 1/4°_{P10}$ to $T - 1/4°$ enhances the magnitude of the SLA HF variability by 10% to almost 100% at most latitudes in zonal average (cf. dashed and solid black lines, top left panel),[5] bringing it much closer to the AVISO reference. Despite this large increase, the HF variability in $T - 1/4°$ remains weaker than observed at midlatitudes (cf. black and green lines). As noted by P10 indeed, ¼° eddy admitting models like ours cannot resolve more than the first deformation radius away from the lowest latitudes; hence, they may underestimate the midlatitude eddy activity generated by baroclinic instability.

P10 have shown that the HF surface variability in $T - 1/4°_{P10}$ was correctly distributed in most regions of the global ocean; at most latitude ranges (black lines, bottom left panel in Fig. 5), this distribution is further improved in $T - 1/4°$. However, certain currents in both

[5] This large increase is consistent with Eden and Dietze's (2009) findings about the suppression of the surface current feedback onto the wind stress.

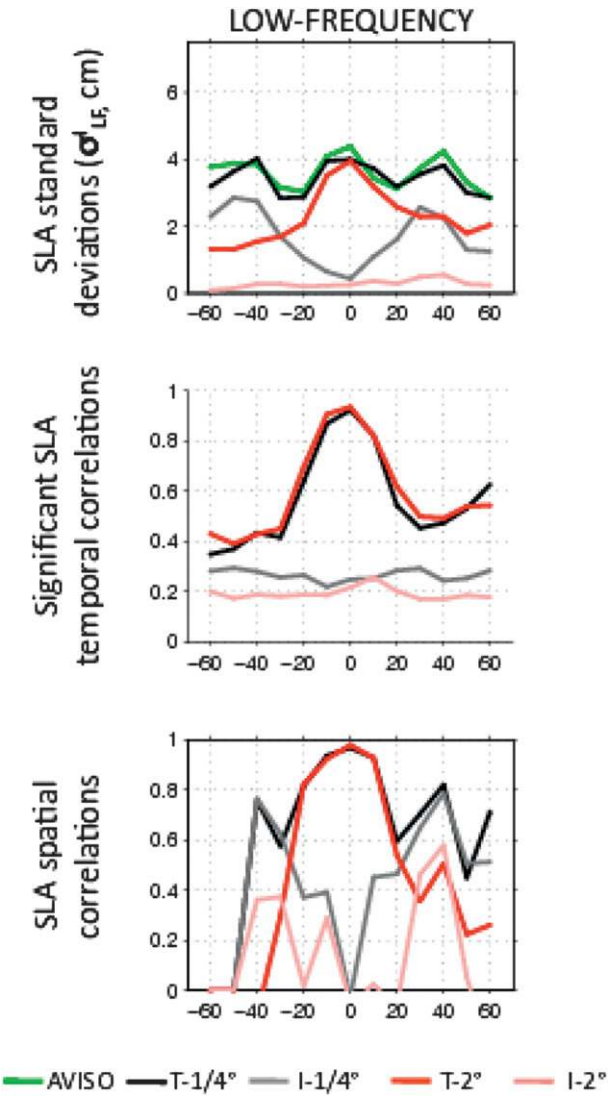

FIG. 6. Skills of the simulations driven by the full DFS4 forcing ($T - 1/4°$ in black, $T - 2°$ in red) and by the seasonal forcing ($I - 1/4°$ in gray, $I - 2°$ in pink) in the LF band as a function of latitude (abscissas). Rows correspond to the same quantities as in Fig. 5. AVISO reference is shown in green.

simulations are locally shifted compared to observations (Fig. 2): the North Atlantic Current (NAC) locally follows the mid-Atlantic Ridge, the Kuroshio does not extend far enough to the east, and the Antarctic Circumpolar Current (ACC) undergoes a localized meridional shift north of the Kerguelen Plateau. Details about these local biases, which are often present in higher-resolution simulations as well, may be found in Barnier et al. (2006).

To summarize at this point, the high-frequency SLA variability in $T - 1/4°$ is typical of eddy-admitting solutions with a few local discrepancies and is more realistic than in $T - 1/4°_{P10}$ in terms of intensity. The reader is referred to P10 for a more detailed description of these local biases.

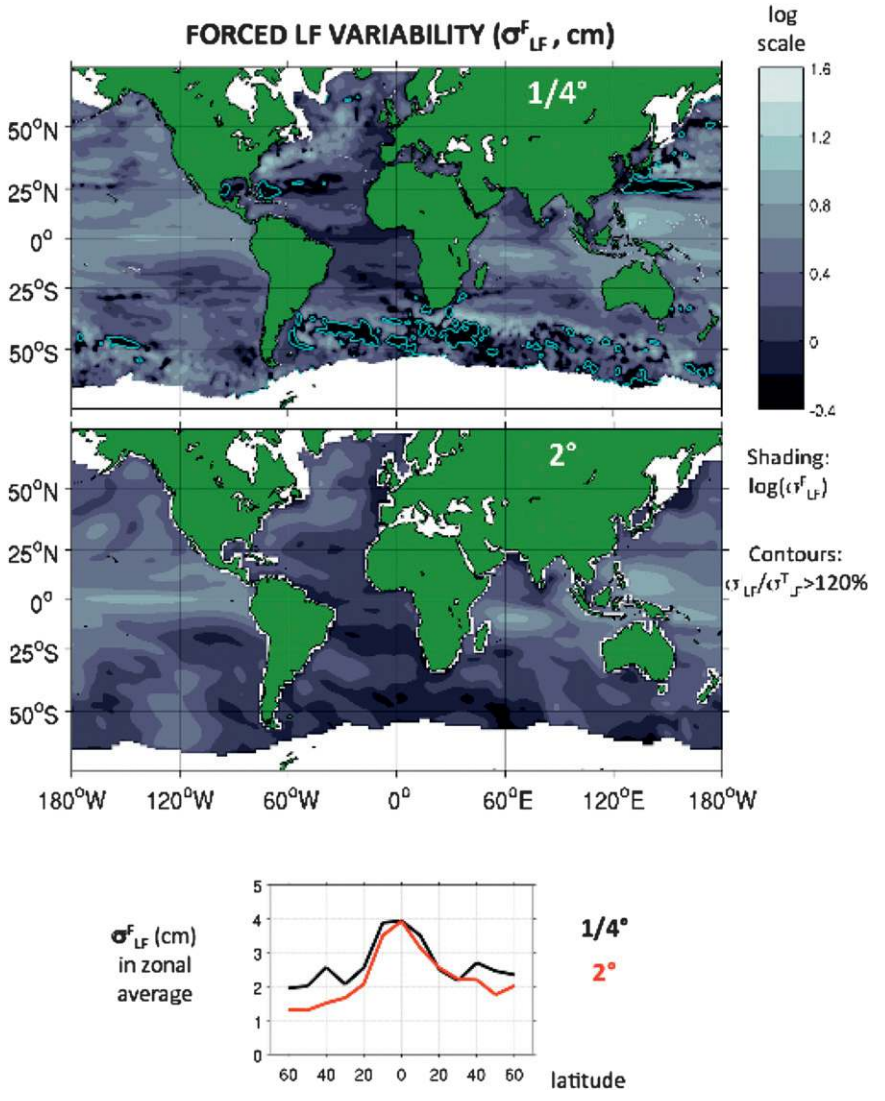

FIG. 7. Maps: Forced variability at LF σ^F_{LF} (log scale, cm) at (top) 1/4° and (middle) 2° resolutions. Contours in (top) enclose areas where the intrinsic SLA variance exceeds the total SLA variance by 20% at 1/4° resolution (this does not happen at 2°); see text for details. (bottom) Zonally averaged LF forced variability σ^F_{LF} as a function of latitude in the 1/4° (black) and 2° (red) cases.

b. *LF variability at ¼°*

The dashed and solid black lines in the right panels in Fig. 5 show at low frequencies how the transition from $T - 1/4°_{P10}$ to $T - 1/4°$ modifies the realism of SLA variabilities. More details about this variability in $T - 1/4°_{P10}$ may be found in P10. The low-frequency SLA variability undergoes a 10%–30% enhancement, which brings its zonally averaged meridional profile remarkably close to the AVISO reference (top right panel). Despite a very small decrease in temporal correlations (middle right panel), the geographical distribution of the LF variability at midlatitudes (bottom right panel) is also improved compared to $T - 1/4°_{P10}$. In other words, the interannual SLA variability is globally improved and compares well with AVISO, in particular in terms of amplitude.

c. *Geographical correspondence between HF and LF variabilities at ¼°*

HF and LF variability maps from each dataset are superimposed in Figs. 2 and 3; their mutual correspondence (e.g., spatial correlations within each dataset) is shown as a function of latitude in Fig. 4. Previous studies have shown [see, e.g., the introduction in Chang et al. (2001)], and the AVISO data confirm (top panel in Fig. 2,

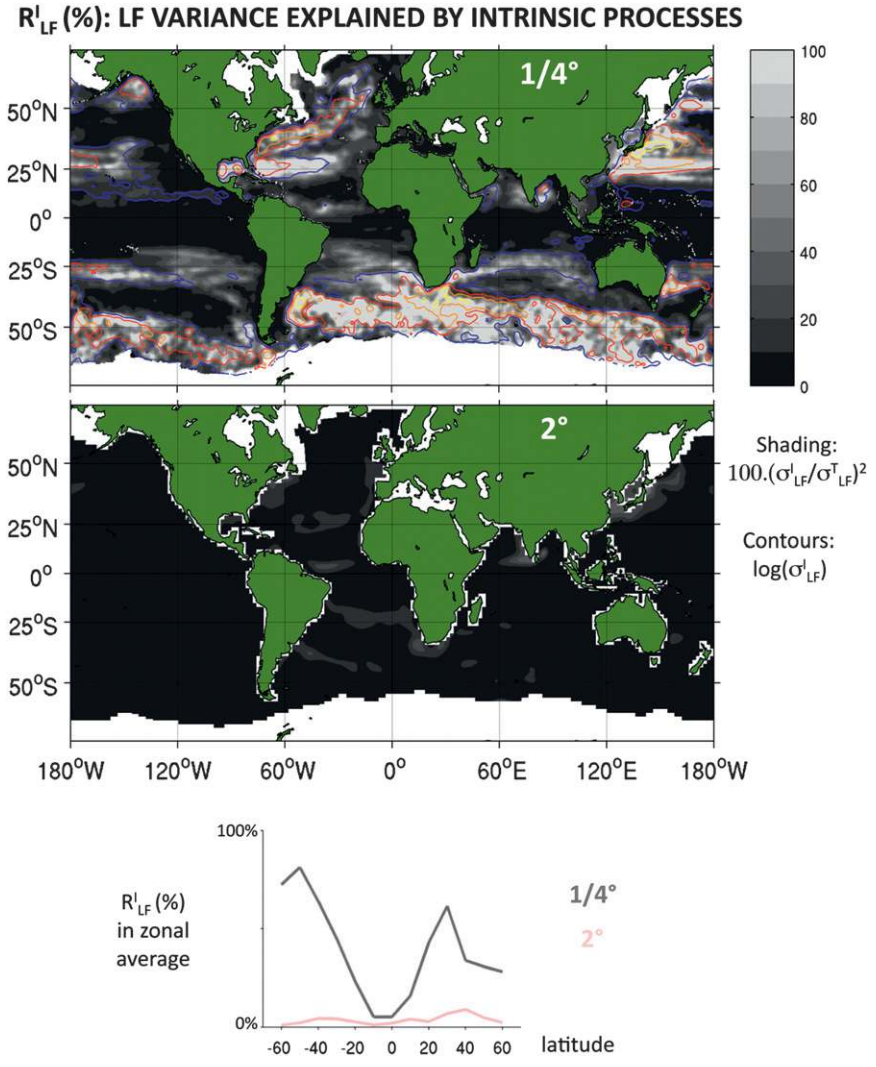

FIG. 8. Maps: Percentage of the LF variance explained by intrinsic processes (R^I_{LF}, shading) at (top) 1/4° and (bottom) 2°. Contours show the LF intrinsic variability in log scale (same colors as in Fig. 2). (bottom) Same percentages averaged zonally and shown as a function of latitude in the 1/4° (red) and 2° (black) cases.

green line in Fig. 4), that most extratropical regions with strong mesoscale variability (HF in contours) also exhibit strong variability at longer time scales, that is, in the interannual (LF, shading) and quasi-annual (not shown; see P10) bands. This is particularly clear along the Gulf Stream (GS), NAC, Kuroshio, ACC, in the Brazil–Malvinas Confluence, in the Agulhas retroflection region, and in the East Australian Current area. P10 showed that a significant part of this localized low-frequency variability is found at scales larger than about 6°.

This observed and simulated correspondence denotes low-frequency fluctuations of both mesoscale activity and regional circulation patterns in the same regions, with probable interactions between both. Namely, eddy energy is drawn from—hence is expected to follow the slow changes of—the regional circulation; in turn, eddies are likely to feed the slow and large-scale variability locally through, for example, Reynolds stress (Berloff et al. 2007) or inverse cascade processes (e.g., Scott and Arbic 2007). Note that the observed maxima of HF and LF variability are much less collocated at low latitudes (spatial correlation falls to 0.15, green line in Fig. 4). This is consistent with the more linear dynamics at work in the equatorial waveguide, where fast and slow waves are more likely to evolve independently than at higher latitudes and to reach maximum amplitudes at different locations.

These observed features are well reproduced in $T - 1/4°$ (middle panel in Fig. 2, black line in Fig. 4). This realistic

correspondence between HF and LF SLA variabilities further confirms the skill of this simulation; its sensitivity to the forcing is further discussed below.

To summarize this section 3, the SLA variability at all time scales in the new $T - 1/4°$ simulation is comparable to its earlier $T - 1/4°_{P10}$ version (extensively described in P10) in terms of phase and spatial distribution, and is much closer to altimetric observations in terms of magnitude. Except in localized areas, our 1/4° model reproduces many features of the real ocean's SLA variability under realistic forcing, in particular at interannual time scales. Its interannual variability without direct interannual forcing is now examined.

4. Intrinsic and forced low-frequency variability at ¼°

We now describe the sea level interannual variability that is generated intrinsically at 1/4° under seasonal forcing (in the $I - 1/4°$ simulation). The forced interannual variability and its contribution relative to the intrinsic component are presented afterward. Note that our diagnostics are local but that the interannual variability might be forced (or intrinsically generated) remotely in space and previously in time. The shading in Figs. 2 and 3 show the maps of total σ^T and intrinsic σ^I variabilities, respectively. Figure 6 shows the zonally averaged profiles of σ, Ct, and Cs for the total and intrinsic variabilities (in black and gray, respectively).

a. Intrinsic LF variability at ¼°

Zonally averaged, significant temporal correlations Ct between low-frequency SLA time series in AVISO and in $I - 1/4°$ (gray line, middle panel of Fig. 6) are much smaller than in the $T - 1/4°$ case (black). This means that the phase of the interannual variability is significantly different from observed, consistent with its intrinsic generation. Note, however, that the decrease in Ct due to the shutoff of interannual forcing is small in the Southern Ocean (where Ct is already small with interannual forcing).

1) Spatial distribution

The top panel in Fig. 6 shows that the intrinsic interannual variability in $I - 1/4°$ (gray line) is very small at low latitudes. Without direct forcing indeed, our numerical ocean cannot generate the main modes of interannual variability that largely involve air–sea coupling in these regions: the El Niño–Southern Oscillation (ENSO; see Philander 1990) or the Indian dipole (e.g., Smith 2000). Relatively linear low-latitude ocean dynamics are also unlikely to locally generate low frequencies through inverse cascade processes. The top panel in Fig. 3 suggests that this weak intrinsic interannual variability may be generated remotely—for example, by the North Brazil Current retroflection or the Indian Ocean Great Whirl—and reach the equator as coastal Kelvin waves. Further regional investigations are needed to test this hypothesis.

The same panel shows that in the extratropics, the largest interannual variability is mostly found in the same areas in $T - 1/4°$ and $I - 1/4°$—that is, along the ACC, in western boundary current extensions (GS, NAC, Kuroshio, East Australian Current), in the Brazil–Malvinas Confluence, and in the Agulhas region. In other words, many extratropical regions where strong interannual variability is found with full forcing (and in AVISO to a large extent) are also regions with strong intrinsic interannual variability. This geographical agreement poleward of 20° is quantified by comparing the gray and black lines in the bottom panel of Fig. 6.

Comparing the contours and shadings superimposed in Figs. 2 and 3 shows that the spatial correspondence between eddy-active areas and regions of large low-frequency variability is stronger in $I - 1/4°$ than in $T - 1/4°$ and in AVISO (this is confirmed by the black, gray, and green lines in Fig. 4). The enhancement of this observed correspondence as the low-frequency forcing is switched off and its confinement in eddy-active midlatitude currents (±40°) demonstrates that the broad-band temporal variability found in SLA along midlatitude eddy-active currents is intrinsically generated in the ocean, rather than forced.

2) Magnitude and regimes

The ratio $R_{\mathrm{LF}}^{I-1/4°}$ between intrinsic ($I - 1/4°$) and total ($T - 1/4°$) interannual SLA variances at 1/4° resolution, defined in section 2c(2), is shown in Fig. 8 (map in the top panel, zonal average as a gray line in the bottom panel). Large and small values of R correspond to predominant contributions of intrinsic and forced interannual variances, respectively. The top panel in Fig. 8 shows that R remains smaller than 20% in the 10°S–10°N band, except in the North Brazil Current retroflection and the area surrounding the Indian Peninsula where ocean-only processes bring the proportion of intrinsic-to-total variability up to 40%–80%. The standard deviation of intrinsic interannual variability is about 2 cm in these areas (top panel in Fig. 3).

Largest values of R are found within the main eddying currents (ACC, Kuroshio, GS, NAC). In zonal average (bottom panel in Fig. 8), 80%–90% of the interannual variability simulated in $T - 1/4°$ is generated intrinsically between the ACC's Sub-Antarctic Front and the sea ice limit (top panel), in particular in its Atlantic and Indian sectors; this feature is further discussed in section 4c below. Relatively large contributions of intrinsic variability

(i.e., 60%–80%) are also found along the path of the GS–NAC and in the North Atlantic subpolar gyre, in the Kuroshio and in the northern Alaskan gyre, and east of Australia. As mentioned above, strong mesoscale activity is also found in these latter regions (contours in the same panel), suggesting the existence of dynamical interactions between both ranges of time scales. Indeed, animations and Hovmöller diagrams from $I - 1/4°$ reveal that both HF and LF SLA variabilities are eddy sized in these regions, further supporting the idea that mesoscale eddies fluctuate over a wide range of time scales near the main currents.

In their Fig. 10b, Taguchi et al. (2007) show in the Kuroshio Extension a ratio $R^* = \sigma^I_{\mathrm{LF}}/\sigma^T_{\mathrm{LF}}$ that relates to our ratio R in a simple way: $R \sim 100\% \times (R^*)^2$. Here R^* was computed from a different model simulation [OGCM for the Earth Simulator (OFES)] at finer resolution ($1/10°$) over a longer, 42 yr, period with a different method. The eastward penetration of our simulated Kuroshio is shorter than observed (Fig. 2) and Taguchi et al.'s (2007) but comparing R^* and R reveals two clear similarities in this region. First, the LF variability in both simulations is largely intrinsic (R^* and R are close to 1 and 100%, respectively) in a broad region surrounding the Kuroshio Extension. Second, R^* and R exceed 1 and 100%, respectively, just poleward of the Kuroshio's variability maximum with peaks locally exceeding 1.1 and 120%, respectively ($R > 120$ within Fig. 7's cyan contours; see below). In other words, these quite different model setups confirm that intrinsic processes largely contribute to the total LF variability in this eddy-active region.

The low-frequency intrinsic variability is not as strong in the quiescent subtropics of both hemispheres; however, it nevertheless exhibits zonally elongated maxima between about 20° and 35°, both in absolute value (Fig. 3) and compared to the total LF variability (Fig. 8). In these latitude bands, which roughly correspond to the equatorward flanks of subtropical gyres, animations and Hovmöller diagrams reveal a different picture than that described in eddy-active regions: the LF intrinsic SLA variability consists of large-scale interannual Rossby wave–like signals that propagate to the west at a few centimeters per second, that are emitted in eastern basins and intensify toward the west throughout the whole 314-yr integration. The scale, phase speed, period, westward intensification, meridional location, and confinement of these first-mode-like baroclinic features are consistent with those found by Hazeleger and Drijfhout (2000) in their idealized study of intrinsic subtropical variability. This qualitative agreement is noteworthy and may indicate similar generation processes; however, the study of these intrinsically generated midlatitude Rossby waves would require a complete characterization of the 3D variability, comparisons with various theories, and perhaps a series of sensitivity experiments in idealized or realistic contexts. This lies beyond the scope of this global description and is left for future studies.

In summary, our results show that a large percentage of the (realistic) SLA interannual variability present in the fully forced case is generated intrinsically: this percentage is actually larger than 40% over half of the global ocean area and exceeds 80% over one-fifth of it.

b. Forced LF variability at 1/4°: Main features

Comparing the black and gray lines in the top panel of Fig. 6 shows that switching on the interannual forcing (i.e., the transition between $I - 1/4°$ and $T - 1/4°$) yields the largest increase in zonally averaged interannual variability between about 20°S and 20°N. The intertropical interannual variability in the real ocean, largely due to ocean–atmosphere interactions that are not explicitly resolved in $T - 1/4°$ [see section 4a(1)], is accurately forced by the DFS4 forcing, in particular at these low latitudes (see section 3b).

Figure 7 shows the forced σ^F variability map at $1/4°$ (top panel) and its zonal average (black line, bottom panel). This map shows that the intertropical interannual variability is markedly influenced by the atmosphere in the Pacific and Indian Oceans, that is, much more than in the Atlantic. This is consistent with the low-latitude distribution of ocean–atmosphere interannual variability modes: ENSO in the Pacific and the Indian dipole (Saji et al. 1999), which are partly connected (Schott and McCreary 2001) and have a larger interannual SST (hence, presumably, SLA) signature than their Atlantic equivalent (Zebiak 1993).

Noting that ENSO and the Pacific decadal oscillation (PDO) have comparable imprints on the North Pacific wind stress curl interannual anomalies (Gershunov and Barnett 1998), and that interannual atmospheric anomalies are stronger in the Pacific than in the Atlantic, the direct influence of the atmosphere on the midlatitude interannual variability [via, e.g., Qiu's (2003) PDO-related mechanism] is expected to be stronger in the Pacific than in the Atlantic. The top panel in Fig. 7 shows that, indeed, the forced midlatitude interannual variability is stronger in the eastern North Pacific ($\sigma^{F-1/4°}_{\mathrm{LF}} > 2.5 - 3$ cm) than in the Atlantic.

Forced interannual variability is found along eastern boundaries, for example, along the northeastern boundary of the Indian Ocean (2 cm). The meridional extent of this maximum suggests that it is forced by equatorial air–sea coupling and propagates northward. Part of this atmospherically driven near-coast interannual variability is also likely to excite westward-propagating Rossby

waves (e.g., along the large-scale local maxima originating from eastern boundaries in the southern Indian and Pacific Oceans) as those mentioned above at midlatitudes.

c. *Intrinsic and forced LF variability at ¼°*

1) Possible relationships

As mentioned above, the cyan contours in the top panel of Fig. 7 enclose regions (mostly in the Southern Ocean and around 25°N) where the LF intrinsic variability found in $I - 1/4°$ exceeds by 20% or more the LF total variability found in $T - 1/4°$. This does not question the validity of our simulations but questions the two simple assumptions made in section 2—that is, 1) the total variability is the sum of the forced and intrinsic components and 2) both components are uncorrelated); at least one of these initial assumptions is invalid there. It is possible that assumption 1 is wrong (e.g., in the highly variable Southern Ocean) because of strong nonlinear interactions between both components. However, it is formally possible that assumption 1 is valid everywhere in $T - 1/4°$ if temporal correlations between the intrinsic and forced components are negative in contoured regions [see Eq. (1)]. In other words, both components might add up everywhere in the fully forced simulation but be partly out of phase in certain regions, hence yielding a total variance that is smaller than the intrinsic variance.

These two simple assumptions may not be formally valid in our complex simulations; however, they proved useful in estimating the forced variability. Further understanding the actual relationships between the forced and intrinsic LF variabilities would certainly require dedicated investigations, preferably in idealized contexts first.

2) Case of the Southern Ocean

Figures 2 and 3 have shown that the observed distribution of the interannual SLA variability in the Southern Ocean is correctly simulated by our ¼° model, with and without interannual forcing (in $T - 1/4°$ and $I - 1/4°$, respectively). Strong interannual variabilities in AVISO and in the latter two simulations are found in eddy-active regions (see Fig. 4), that is, along ACC fronts. The top panel in Fig. 9 shows the interannual SLA variability simulated with full forcing ($\sigma_{\mathrm{LF}}^{T-1/4°}$) and black dots show the location of its maximum at each longitude. Away from the Kerguelen Plateau (75°–90°E), this maximum follows the Subtropical Front between about 30° and 65°E and the Sub-Antarctic Front between about 65° and 140°E [based on the map by Orsi et al. (1995)]. Figure 9's bottom two panels show the contributions of the intrinsic and forced interannual variabilities at given meridional distances (ordinates) from the fully forced variability maximum shown as black dots in the top panel.

The right bottom panel in Fig. 9 shows that the intrinsic variability maximum ($I - 1/4°$, red peak) is slightly displaced southward (50 km) compared to the total variability maximum ($T - 1/4°$, black peak). Although set at first order by the topography (Sallée et al. 2008), the position of the ACC fronts may vary on interannual time scales, either because of the forcing (Fyfe and Saenko 2006) or just intrinsically. As the front constitutes a large gradient in SSH, forced and intrinsic shifts in its position should induce large SLA variabilities there. The forced and intrinsic variabilities, indeed, reach their (comparable) maximum amplitudes close to the main front.

Interestingly, most of the interannual SLA variability is forced by the atmosphere north of the total maximum (therefore including the area where the Subantarctic Mode Water is formed and subducted). On the contrary, the interannual SLA variability is almost fully intrinsic (red line) south of the total maximum (black peak); this is consistent with the aforementioned small temporal correlations and with their weak sensitivity to the presence of interannual forcing (middle panel in Fig. 6). The left bottom panel in Fig. 9 as well as Figs. 3 and 7 exhibit this meridional contrast over most of this 130° range of longitude.

The origin of this marked contrast is not clear, but we offer a hypothesis. The maximum in LF variability shown as black dots in the top panel of Fig. 9 approximately follows the southern edge of the so-called Southern Hemisphere supergyre [see Fig. 3 in Ridgway and Dunn (2007)]. This wide circulation pattern is predicted by Sverdrup dynamics (de Ruijter 1982) and is hence presumably sensitive to low-frequency fluctuations of the large-scale wind stress curl. Our results show that, indeed, the interannual SLA variability north of the black dots has large spatial scales (larger than 6°, not shown) and is mostly forced by the atmosphere. In the ACC south of this subtropical cell, the interannual SLA variability is not likely to be governed by the Sverdrup balance (Rintoul et al. 2001; LaCasce and Isachsen 2010), and hence it is presumably not to be structured at the basin scale. Indeed, we find that the interannual SLA variability south of the maximum is largely independent of the forcing and has much smaller scales than north of it.

To summarize, our ¼° simulations exhibit sharp changes in the origin and spatial scales of the SLA interannual variability where subtropical Sverdrup-based dynamics change into circumpolar dynamics. More investigation and additional sensitivity experiments should help verify whether these concomitant transitions are linked physically.

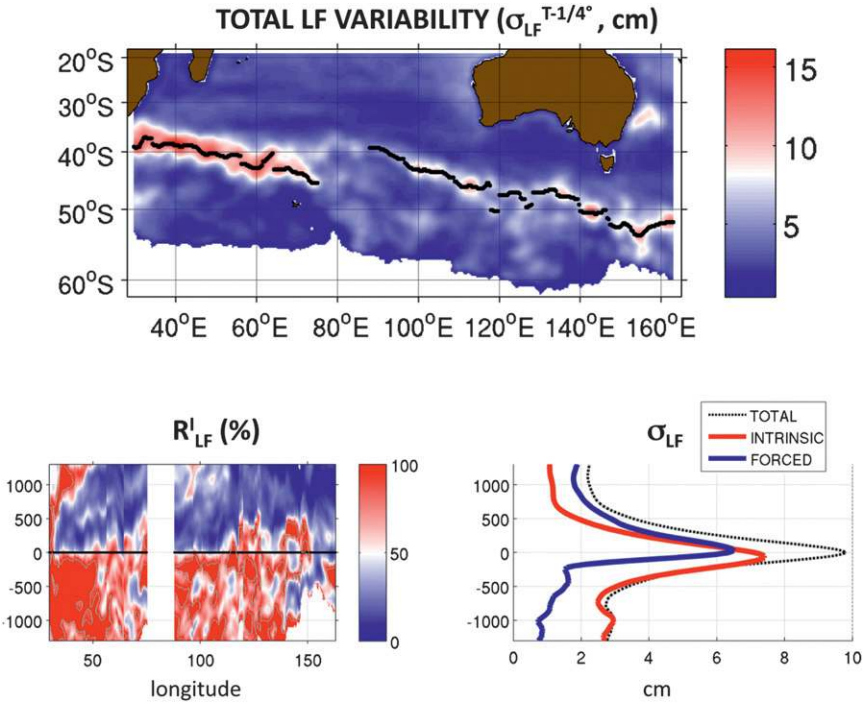

FIG. 9. The LF SLA variability in the ACC at 1/4° resolution. (top) Total variability ($\sigma_{\mathrm{LF}}^{T-1/4^\circ}$, cm). The sinuous black line follows the maximum of this field in $T - 1/4^\circ$ at each longitude (excluding the Kerguelen Plateau) and corresponds to ordinate 0 in the other two panels. (bottom left) Percentage of variance explained by the intrinsic component (R^I_{LF}, color), as a function of longitude (abscissas) and of the meridional distance to the maximum of $\sigma_{\mathrm{LF}}^{T-1/4^\circ}$ (ordinate, km); the Kerguelen region is omitted; contours as in Fig. 7. (bottom right) Total (black), intrinsic (red), and forced (blue) LF standard deviations are averaged between 30° and 163°E (omitting the Kerguelen Plateau) at constant distances from the maximum of $\sigma_{\mathrm{LF}}^{T-1/4^\circ}$, and shown as a function of this distance.

5. Role of resolved versus parameterized eddies

We now isolate from the 2° simulations ($T - 2^\circ$ and $I - 2^\circ$) the intrinsic and forced components of the interannual SLA variability, and compare them with their 1/4° equivalents. Our main purpose here is to evaluate the possible sensitivity of these components to the explicit (although partial) resolution of mesoscale eddies at 1/4° versus their parameterization at 2°. The total interannual variability in $T - 2^\circ$ is evaluated against altimetry (using $T - 2^\circ_{P10}$ as a reference for conciseness) in section 5a below. Its intrinsic and forced components are described and compared to their $T - 1/4^\circ$ counterparts afterward.

a. Assessment of SLA variability in $T - 2^\circ$

The red solid lines lie on or above red dashed lines in all panels of Fig. 5. This means that at 2° resolution as well, the forcing update has a beneficial (or neutral) impact on the magnitude and distribution of SLA variability at all time scales. Therefore, the $T - 2^\circ$ interannually forced simulation has globally more skill than its earlier "P10" version in reproducing the observed SLA variability at all time scales and differs from $T - 1/4^\circ$ in the way described in P10 regardless of forcing update. We now focus on the comparison of $T - 2^\circ$ and $I - 2^\circ$ to isolate the intrinsic and forced variabilities simulated at 2°.

b. Intrinsic and forced low-frequency variability at 2°

1) INTRINSIC LF VARIABILITY AT 2°

The maps in Fig. 3, the top panel of Fig. 6 (gray and pink lines), and Fig. 8 show that the transition from eddying to laminar regimes almost suppresses the intrinsic variability, bringing its contribution to the total interannual variability to very small percentages (smaller than 3% over half of the global ocean). This confirms that (even partly) resolved nonlinear eddies (and/or reduced dissipation) play a critical role in generating (and/or not dissipating) intrinsic LF variability. Although much smaller, the contribution R^I_{LF} of intrinsic variability to the total reaches 20%–30% at 2° in a few regions where it is large at 1/4°, suggesting that noneddying

processes (e.g., large-scale Rossby or Kelvin waves) are involved there. However, in areas of strong eddy activity (ACC, western boundary currents), the decrease in the intrinsic contribution due to the coarser resolution is greater, further supporting the large involvement of nonlinear eddy processes in producing intrinsic variability.

2) Forced LF variability at 2°

The shading in the middle panel of Fig. 7 shows the forced LF variability at 2°: the large-scale patterns of this component appears much less sensitive than the intrinsic component to the decrease in model resolution. Differences between $\sigma^{F-1/4^\circ}$ and σ^{F-2° are found in the Southern Ocean; nonetheless, the 2° counterpart of Fig. 9's bottom right panel (not shown) indicates that the forced variability remains stronger north of the ACC front than south of it at 2° as well. This weak sensitivity of the forced variability to resolution strongly suggests that at first order in our forced simulations, and unlike the intrinsic component, the forced LF variability involves relatively linear dynamics; these include, for example, Rossby waves, Kelvin waves, Sverdrup-type responses, or wind-forced topographically trapped Taylor columns that are likely responsible for the southeastern Pacific maximum (Webb and de Cuevas 2003) visible at both resolutions.

Besides this general agreement, the zonally averaged forced LF variability (bottom panel in Fig. 7) is up to 20% larger at ¼° than at 2° at mid- and high latitudes, this is, where eddies are most energetic. Two arguments may be proposed to explain this difference. First, horizontal viscosity is much reduced at ¼° and may have less impact on the dissipation of horizontal motions, including forced motions. Second, the main currents—such as the ACC (see above), the Gulf Stream, or the Kuroshio—have a stronger signature in SSH gradients at ¼°; interannual migrations of these fronts due to the forcing and will therefore yield a larger forced SLA variability at ¼°.

6. Conclusions and discussion

The main purpose of this study was to estimate and describe the sea level expression of intrinsic and forced variabilities in the ocean at interannual time scales in a global, realistic context (using a ¼° eddying OGCM with realistic geometry, initial condition, forcing, etc.). We have compared the interannual ($T > 18$ months) sea level anomalies (SLAs) simulated with two different forcing functions: a realistic forcing with temporal scales ranging from 12 h to decades (simulation $T - ¼°$) and the climatological seasonal cycle derived from the former (simulation $I - ¼°$).

A quantitative comparison of the $T - ¼°$ simulation with AVISO observations demonstrated the realism of the total sea surface variability (global distribution, magnitude) between 1993 and 2004, in particular at interannual time scales. The intrinsic interannual variability was diagnosed in $I - ¼°$, and the forced component was deduced by subtracting the intrinsic from the total variance fields. Our main results concerning the intrinsic and forced components are summarized below.

- Without any interannual forcing, $I - ¼°$ generates an intrinsic SLA variance that exceeds 40% of its fully forced counterpart over half of the global ocean. This intrinsic contribution is largest in strong eddy-active regions: its zonal average reaches 70%–75% south of the ACC and 50%–55% over the main western boundary currents and their extensions. Since their phase is not constrained by the forcing, correlation coefficients between intrinsic SLA fluctuations and AVISO time series at low frequency are small everywhere. The intrinsic component is weaker in absolute value but remains large in proportion within the 20°–35° latitude band in both hemispheres; there, preliminary diagnostics reveal the presence of interannual Rossby waves continuously emitted despite the absence of direct interannual forcing.
- The LF variability is largely influenced by the atmosphere (i.e., forced by it in the absence of air–sea coupling) in the tropical Pacific and Indian Oceans. The weaker interannual variability forced at low latitudes in the Atlantic (and perhaps at higher latitudes too) is likely due to the imprint of ENSO, which is largest in the Pacific and Indian Oceans. The strongest direct influence of the atmosphere on interannual SLAs far from the equator is found in the northeastern Pacific.
- As predicted by idealized studies and as seen in altimeter observations, the interannual variability is strong where mesoscale eddies are strong in our fully forced simulation. In other words, unstable currents exhibit a strong broadband temporal variability. This spatial correspondence is even clearer without direct interannual forcing ($I - ¼°$), strongly suggesting the oceanic (eddy driven) origin of this interannual variability. The interannual SLA variability is largely intrinsic and has a broad range of spatial scales south of the ACC in the Indian Ocean Basin; in contrast, this variability is mostly forced by the atmosphere north of it and has typical scales larger than 6°. Explaining this sharp meridional contrast is left for the future.
- The intrinsic interannual variability is almost absent from our 2° simulations; however, the forced interannual

variability is less sensitive to model resolution. This reaffirms that in our simulations, mesoscale eddies and nonlinear processes are likely to play a major role in producing intrinsic variability, and suggests that they are weakly involved in the SLA response to direct atmospheric forcing (which is probably linear at first order). The chaotic behavior of this eddy-driven intrinsic component may explain why temporal correlations between AVISO and fully forced simulations decrease as resolution increases, both in the present study and in Penduff P10.

Our results have several implications regarding the interannual variability simulated by ocean models at various resolutions. As seen in the $T - 2° \rightarrow T - 1/4°$ transition, resolving eddies 1) brings the distribution and magnitude of the total interannual variability very close to observational estimates, 2) does not modify much the large-scale distribution and magnitude of the *forced* variability but 3) strongly enhances the *intrinsic* component. Since the $T - 1/4°$ simulation compares much better than $T - 2°$ with AVISO observations, it is likely that the 1/4° diagnostics presented here have some relevance for the real ocean: a substantial part of the real interannual SLA variability is probably generated by the ocean under the sole influence of mean and seasonal atmospheric forcing.

We also showed that the extratropical variability simulated by our Intergovernmental Panel on Climate Change (IPCC)-class coarse-resolution model driven by the same interannual forcing amounts to only a fraction of the observed variability, mostly because the intrinsic variability generated by laminar dynamics (and parameterized eddy fluxes) is very weak. In other words, laminar ocean models are much less influenced by chaotic variability than eddying models. At least within regions with a substantial intrinsic variability, the predictability of interannual variability (i.e., in agreement with the phase of observed events) may therefore be degraded as the resolution increases in ocean-only high-resolution forecasts (like in our $T - 1/4°$ hindcast). This advocates for ensemble high-resolution ocean forecasts.

Berloff and McWilliams (1999) and others have shown in idealized setups that increasing Reynolds numbers (via, e.g., smaller viscosities and/or finer resolutions) tend to enhance the magnitude and chaotic character of the intrinsic variability; is there evidence of such a sensitivity within the existing range of eddying OGCM simulations? ''Eddy resolving'' (e.g., 1/10°) OGCMs generally produce more realistic mean states and more mesoscale activity than their ''eddy admitting'' (e.g., 1/4°) counterparts (e.g., Hurlburt and Hogan 2000; Smith et al. 2000; Treguier et al. 2005). At interannual time scales in the Kuroshio region, Taguchi et al. (2007)'s 1/10° global simulations and our 1/4° counterparts do not differ much regarding the magnitude of their intrinsic variabilities, total variabilities, and ratios between both. This regional resemblance suggests that these 1/4° and 1/10° models capture comparable features of total and intrinsic interannual variabilities in this particular region, although this agreement cannot be assessed at global scale (Taguchi et al.'s study is regional). It is also likely that the detailed structure of the intrinsic variability depends on the model considered. Investigating these dependencies to model parameters and resolution remains to be done at regional and global scales.

The absence of air–sea coupling allowed us to separate forced and intrinsic ocean variabilities. Brightly shaded regions in the top panel in Fig. 8 locate many areas where the low-frequency SLA variability is mostly intrinsic. One may expect that in such regions, low-frequency intrinsic SLA fluctuations have signatures in SST that could then *force* low-frequency atmospheric fluctuations. At least in these regions, low-frequency atmospheric variability might therefore be driven by slowly varying SST changes of oceanic origin, which are not resolved in coarse-resolution ocean models. Western boundary current extensions (Berloff and McWilliams 1999) and large areas of the Southern Ocean are good candidates for such a scenario. Identifying the implications of our results for the fully coupled climate system is left for future studies.

Like the forced ocean variability (Sverdrup-type responses, Rossby and Kelvin waves, etc.), the intrinsic variability has subsurface, multivariate signatures [see idealized studies by, e.g., Spall (1996); Hogg and Blundell (2006)] that we ignored, mostly because observations with the adequate space–time span are restricted to the surface. Although certain important climate indices like the meridional overturning circulation (MOC) (Bingham and Hughes 2009), the transport of major currents (Kelly 1991) or overflows (Hoyer and Quadfasel 2001) have a signature in SLA, we did not investigate their intrinsic variations since we lack adequate observations. Dedicated observational and modeling studies are thus needed to monitor and understand the intrinsic variability of subsurface fields and climate-relevant quantities. As also stated by Berloff and McWilliams (1999) in their conclusion, the (intrinsic) low-frequency variability is poorly known in the real ocean; quantitative estimates about its manifestations and magnitude in the real ocean requires more ''realistic'' simulations than those used in process studies. The present study may be seen as such an attempt to provide process-oriented studies with

a more realistic context, in close connection with real observations.

Acknowledgments. Suggestions made by Pavel Berloff and an anonymous reviewer led to significant improvement of this paper. This work is a contribution of the Drakkar project, which is supported by the Centre National d'Etudes Spatiales (CNES) through the Ocean Surface Topography Science Team (OST/ST), by the Centre National de la Recherche Scientifique (CNRS), the Institut National des Sciences de l'Univers (INSU), and the Groupe Mission Mercator Coriolis (GMMC). Partial support of the European Commission under Grant Agreement FP7-SPACE-2007-1-CT-218812-MYOCEAN is also gratefully acknowledged. Computations presented in this study were performed at Institut du Développement et des Ressources en Informatique Scientifique (IDRIS) and the Centre Informatique National de l'Enseignement Supérieur (CINES). The T − ¼° (ORCA025-MJM01) simulation was performed at CINES as part of the Grands Challenges GENCI/CINES 2008. Most of this research was done during TP's stay at the Department of Oceanography at FSU, now named the Earth, Ocean and Atmospheric Science Department. TP wishes to acknowledge a number of interesting conversations with Peter Rhines, Michael Ghil, Greg Holloway, Pavel Berloff, and Julie Deshayes.

APPENDIX A

Periods

We aim to illustrate from SLA fields some relationships between the mesoscale activity (HF band) and the intrinsic low-frequency variability (LF band) in the $I - ¼°$ simulation. This requires the availability of LF and HF time series simultaneously, which only occurs after 300 yr of spinup (only monthly $T - ¼°$ outputs are available before year 300). We verified that the detrended interannual variabilities $\sigma_{\mathrm{LF}}^{I-1/4^\circ}$ computed over 23 successive 12-yr periods vary moderately throughout the last 276 yr of $I - ¼°$: the standard deviation of this 23-member time series remains below 10% of its mean, peaking at 20% at 30°N. In other words, comparing detrended SLA variabilities in $I - ¼°$ and $T - ¼°$ over 12-yr periods chosen after different spinup durations (301 and 35 yr, respectively) is consistent, and also allows a comparison between HF and LF variabilities in $I - ¼°$. In summary, $T - ¼°$ statistics are computed over 1993–2004; they are compared in section 3 to AVISO statistics computed over the same period and in section 4 to $I - ¼°$ statistics computed over years 302–13.

APPENDIX B

Detrending

Our main aim is to compare observed, total, intrinsic, and forced LF variabilities of SLA at low and high frequency over the same range of available time scales, that is, over the 12-yr period that is common to AVISO and interannual runs. Linear trends were removed from all LF collocated (observed and simulated) local SLA time series before computing and comparing statistics (standard deviations, correlations). Indeed, some components of local trends may differ within our seven-member SLA dataset for three main reasons. First, part of these trends might simply come from the truncation of interdecadal oscillations, which are present in AVISO, but are likely affected by the limited duration of model spinups. Second, the potentially intrinsic (i.e., chaotic) component of interdecadal variabilities may induce SLA fluctuations with different phases in AVISO and each simulation, hence yield arbitrary trends in individual 12-yr time series and contaminate statistics. Third, the 12-yr truncation of long-term, forced climate trends present in AVISO may be altered by spurious SLA drifts in forced simulations because freshwater fluxes are uncertain (Béranger et al. 2006). In summary, we removed the linear trends from all LF time series because their origins in simulations and in observations may be different, hence cannot be compared consistently. Beyond these reasons, removing trends also focuses our analysis on a range of time scales that is ''resolved'' in every 12-yr time series. Note, however, that this removal had only a small quantitative impact on our results.[B1]

REFERENCES

Barnier, B., and Coauthors, 2006: Impact of partial steps and momentum advection schemes in a global circulation model at eddy-permitting resolution. *Ocean Dyn.,* **56,** 543–567, doi:10.1007/s10236-006-0082-1.

Béranger, K., B. Barnier, S. Gulev, and M. Crépon, 2006: Comparing 20 years of precipitation estimates from different sources over the world ocean. *Ocean Dyn.,* **56,** 104–138.

Berloff, P. S., and J. C. McWilliams, 1999: Large-scale, low-frequency variability in wind-driven ocean gyres. *J. Phys. Oceanogr.,* **29,** 1925–1949.

[B1] P10 chose not to detrend SLA time series because their four simulations were forced identically and were compared to AVISO after the same period of spinup. This choice explains the small differences found between the dashed lines in Fig. 5 and their counterpart (black and magenta lines) in P10's Fig. 6.

——, W. Dewar, S. Kravtsov, and J. C. McWilliams, 2007: Ocean eddy dynamics in a coupled ocean–atmosphere model. *J. Phys. Oceanogr.,* **37,** 1103–1121.

Biastoch, A., C. Böning, and J. Lutjeharms, 2008: Agulhas leakage dynamics affects decadal variability in Atlantic overturning circulation. *Nature,* **456,** 489–492.

Bingham, R. J., and C. W. Hughes, 2009: Signature of the Atlantic meridional overturning circulation in sea level along the east coast of North America. *Geophys. Res. Lett.,* **36,** L02603, doi:10.1029/2008GL036215.

Brodeau, L., B. Barnier, T. Penduff, A.-M. Treguier, and S. Gulev, 2010: An ERA40-based atmospheric forcing for global ocean circulation models. *Ocean Modell.,* **31,** 88–104.

Cabanes, C., T. Huck, and A. Colin de Verdière, 2006: Contributions of wind forcing and surface heating to interannual sea level variations in the Atlantic Ocean. *J. Phys. Oceanogr.,* **36,** 1739–1750.

Cessi, P., and S. Louazel, 2001: Decadal oceanic response to stochastic wind forcing. *J. Phys. Oceanogr.,* **31,** 3020–3029.

Chang, K.-I., M. Ghil, K. Ide, and C.-C. A. Lai, 2001: Transition to aperiodic variability in a wind-driven double-gyre circulation model. *J. Phys. Oceanogr.,* **31,** 1260–1286.

de Ruijter, W., 1982: Asymptotic analysis of the Agulhas and Brazil Current systems. *J. Phys. Oceanogr.,* **12,** 361–373.

Dewar, W., 2001: On ocean dynamics in midlatitude climate. *J. Climate,* **14,** 4380–4397.

——, 2003: Nonlinear midlatitude ocean adjustment. *J. Phys. Oceanogr.,* **33,** 1057–1082.

Dijkstra, H. A., and M. Ghil, 2005: Low-frequency variability of the large-scale ocean circulation: A dynamical systems approach. *Rev. Geophys.,* **43,** RG3002, doi:10.1029/2002RG000122.

Eden, C., and H. Dietze, 2009: Effects of mesoscale eddy/wind interactions on biological new production and eddy kinetic energy. *J. Geophys. Res.,* **114,** C05023, doi:10.1029/2008JC005129.

Fyfe, J. C., and O. A. Saenko, 2006: Simulated changes in the extratropical Southern Hemisphere winds and currents. *Geophys. Res. Lett.,* **33,** L06601, doi:10.1029/2005GL025332.

Gershunov, A., and T. Barnett, 1998: Interdecadal modulation of ENSO teleconnections. *Bull. Amer. Meteor. Soc.,* **79,** 2715–2726.

Hall, N., B. Barnier, T. Penduff, and J.-M. Molines, 2004: Interannual variation of Gulf Stream heat transport in a high resolution model forced by reanalysis data. *Climate Dyn.,* **23,** 341–351.

Hazeleger, W., and S. Drijfhout, 2000: A model study on internally generated variability in subtropical mode water formation. *J. Geophys. Res.,* **105,** 13 965–13 979.

Hogg, A. M., and J. Blundell, 2006: Interdecadal variability of the Southern Ocean. *J. Phys. Oceanogr.,* **36,** 1626–1645.

Hoyer, J. L., and D. Quadfasel, 2001: Detection of deep overflows with satellite altimetry. *Geophys. Res. Lett.,* **28,** 1611–1614.

Hurlburt, H. E., and P. J. Hogan, 2000: Impact of $1/8°$ to $1/64°$ resolution on Gulf Stream model-data comparisons in basin-scale subtropical Atlantic Ocean models. *Dyn. Atmos. Oceans,* **32,** 283–330.

Jiang, S., F.-F. Jin, and M. Ghil, 1995: Multiple equilibria, periodic, and aperiodic solutions in a wind-driven, double-gyre, shallow-water model. *J. Phys. Oceanogr.,* **25,** 764–786.

Kelly, K. A., 1991: The meandering Gulf Stream as seen by the Geosat altimeter: Surface transport, position, and velocity variance from 73° to 46°W. *J. Geophys. Res.,* **96,** 16 712–16 738.

LaCasce, J. H., and P. E. Isachsen, 2010: The linear models of the ACC. *Prog. Oceanogr.,* **84,** 139–157.

Madec, G., and the NEMO Team, 2008: NEMO ocean engine. Institut Pierre-Simon Laplace Note du Pôle de Modélisation 27.

Orsi, A. H., T. Whitworth III, and W. D. Nowlin Jr., 1995: On the meridional extent and fronts of the Antarctic Circumpolar Current. *Deep-Sea Res.,* **42,** 641–673.

Pacanowski, R., 1987: Effect of equatorial currents on surface stress. *J. Phys. Oceanogr.,* **17,** 833–838.

Penduff, T., B. Barnier, W. K. Dewar, and J. J. O'Brien, 2004: Dynamical response of the oceanic eddy field to the North Atlantic Oscillation: A model–data comparison. *J. Phys. Oceanogr.,* **34,** 2615–2629.

——, M. Juza, L. Brodeau, G. C. Smith, B. Barnier, J.-M. Molines, A.-M. Treguier, and G. Madec, 2010: Impact of global ocean model resolution on sea-level variability with emphasis on interannual time scales. *Ocean Sci.,* **6,** 269–284.

Philander, S. G. H., 1990: *El Niño, La Niña and the Southern Oscillation*. Academic Press, 289 pp.

Pierini, S., 2006: A Kuroshio Extension system model study: Decadal chaotic self-sustained oscillations. *J. Phys. Oceanogr.,* **36,** 1605–1625.

Qiu, B., 2003: Kuroshio Extension variability and forcing of the Pacific decadal oscillations: Responses and potential feedback. *J. Phys. Oceanogr.,* **33,** 2465–2482.

Ridgway, K. R., and J. R. Dunn, 2007: Observational evidence for a Southern Hemisphere oceanic supergyre. *Geophys. Res. Lett.,* **34,** L13612, doi:10.1029/2007GL030392.

Rintoul, S. R., C. W. Hughes, and D. Olbers, 2001: The Antarctic Circumpolar Current system. *Ocean Circulation and Climate: Observing and Modelling the Global Ocean,* G. Siedler, J. Church, and J. Gould, Eds., International Geophysics Series, Vol. 77, Academic Press, 271–302.

Saji, N., B. Goswami, P. Vinayachandran, and T. Yamagata, 1999: A dipole in the tropical Indian Ocean. *Nature,* **401,** 360–363.

Sallée, J. B., K. Speer, and R. Morrow, 2008: Southern Ocean fronts and their variability to climate modes. *J. Climate,* **21,** 3020–3039.

Schott, F. A., and J. P. McCreary Jr., 2001: The monsoon circulation of the Indian Ocean. *Prog. Oceanogr.,* **51,** 1–123.

Scott, R. B., and B. K. Arbic, 2007: Spectral energy fluxes in geostrophic turbulence: Implications for ocean energetics. *J. Phys. Oceanogr.,* **37,** 673–688.

Simonnet, E., M. Ghil, K. Ido, and R. Temam, 2003: Low-frequency variability in shallow-water models of the wind-driven ocean circulation. Part II: Time-dependent solutions. *J. Phys. Oceanogr.,* **33,** 729–752.

——, ——, and H. A. Dijkstra, 2005: Homoclinic bifurcations in the quasi-geostrophic double-gyre circulation. *J. Mar. Res.,* **63,** 931–956.

Smith, R., M. Maltrud, F. Bryan, and M. Hecht, 2000: Numerical simulation of the North Atlantic Ocean at $1/10°$. *J. Phys. Oceanogr.,* **30,** 1532–1561.

Smith, T. M., 2000: Tropical Pacific sea level variations (1948–98). *J. Climate,* **13,** 2757–2769.

Spall, M., 1996: Dynamics of the Gulf Stream/deep western boundary current crossover. Part II: Low-frequency internal oscillations. *J. Phys. Oceanogr.,* **26,** 2169–2182.

Taguchi, B., S.-P. Xie, N. Schneider, M. Nonaka, H. Sasaki, and Y. Sasai, 2007: Decadal variability of the Kuroshio Extension:

Observations and an eddy-resolving model hindcast. *J. Climate,* **20,** 2357–2377.

Treguier, A.-M., S. Theetten, E. Chassignet, T. Penduff, R. Smith, L. Talley, J. O. Beismann, and C. Böning, 2005: The North Atlantic subpolar gyre in four high-resolution models. *J. Phys. Oceanogr.,* **35,** 757–774.

von Storch, H., and F. W. Zwiers, 1999: *Statistical Analysis in Climate Research*. Cambridge University Press, 484 pp.

Webb, D. J., and B. A. de Cuevas, 2003: The region of large sea surface height variability in the southeast Pacific Ocean. *J. Phys. Oceanogr.,* **33,** 1044–1056.

Wirth, A., J. Willebrand, and F. Schott, 2002: Variability of the Great Whirl from observations and models. *Deep-Sea Res. II,* **49,** 1279–1295.

Zebiak, S., 1993: Air–sea interaction in the equatorial Atlantic region. *J. Climate,* **6,** 1567–1568.